

Yang, F., et al., 2024, Excessive subsidence of oceanic basins caused by recycled oceanic crust in the mantle source: A new perspective on the oceanic topography within Southeast Asia: *Geology*, <https://doi.org/10.1130/G52079.1>

Supplemental Material

These files include analytical methods, photographs of samples, descriptions of melt inclusion corrections, estimation of the amount of recycled oceanic crust in the South China Sea MORB source, details of numerical modeling, and data for samples and standards used in this study.

Including:

Figures S1–S8

Tables S1–S6

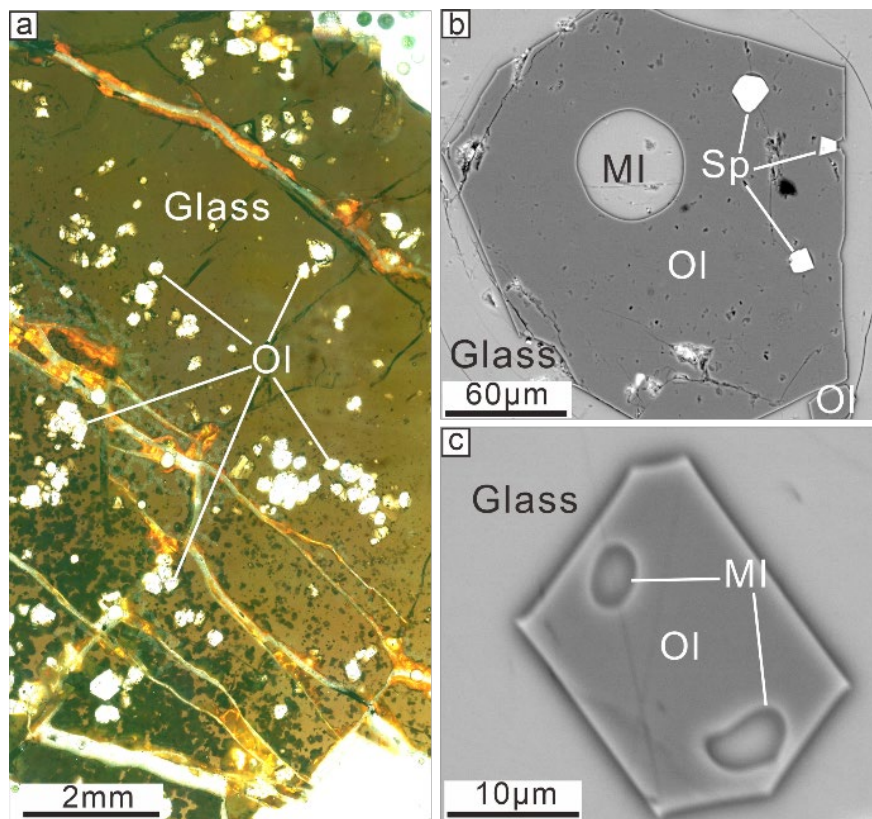
SUPPLEMENTARY MATERIAL

1. Analytical Methods

The analyses were performed at the Guangzhou Institute of Geochemistry, Chinese Academy of Sciences. Major and minor elements in olivines, melt inclusions (MIs), and glasses were analyzed *in situ* using a Cameca SXFive FE Electron Probe Microanalyzer. Olivines were analyzed using a 15 kV accelerating voltage and 40 nA beam current (Yang et al., 2019). MIs and the host glass were analyzed at 15 kV, 20 nA with a beam size of 3 μm . The trace element concentrations of the MIs and the host glass were measured using an ELEMENT XR ICP-SF-MS (Thermo Fisher Scientific) coupled with a 193-nm (ArF) Resonetics RESolution M-50 laser ablation system. A beam size of either 24 μm or 32 μm , repetition rate of 6 Hz, and energy density of $\sim 5 \text{ J cm}^{-2}$ were applied during the analysis, following Zhang et al. (2019).

2. Melt Inclusion Corrections

The melt inclusions (MIs) were collected from euhedral olivine phenocrysts in quenched glasses (Fig. S1). We analyzed naturally quenched MIs hosted by euhedral olivines. Back scatter electron (BSE) images show that all the MIs are glassy without any daughter minerals.



24

25

26 *Figure S1. Photographs of the studied samples. (a) Basaltic glass hosting euhedral*
 27 *olivines (transmitted and reflected light); (b) BSE image of a relatively large euhedral*
 28 *olivine that hosts a rounded melt inclusion (~50 µm in diameter) and some euhedral*
 29 *spinel inclusions; (c) BSE image of a relatively small olivine that hosts oval-shaped*
 30 *melt inclusions. Abbreviations: olivine (Ol), spinel (Sp), and melt inclusion (MI).*

31

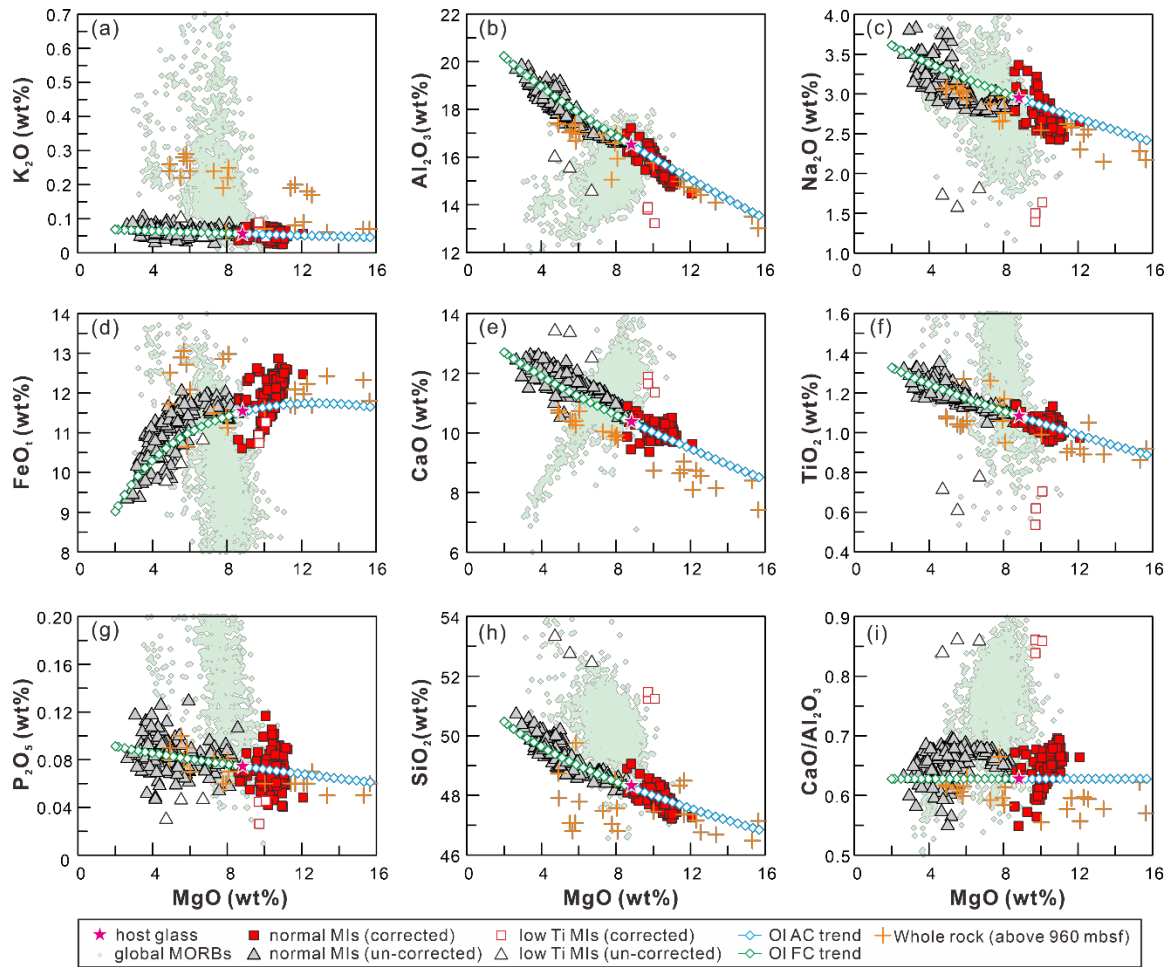


Figure S2. Plots of major element contents and $\text{CaO}/\text{Al}_2\text{O}_3$ ratios versus MgO contents of melt inclusions and host glasses. Both the measured compositions of MIs (uncorrected) and corrected compositions (corrected) of MIs in equilibrium with host olivine are shown. Whole-rock compositions of basalts from Hole U1431E (Zhang et al., 2018) and olivine accumulation (Ol AC) and fractionation (Ol FC) trends are shown for comparison. The melt inclusions are separated into two groups: normal and low-Ti types (f). The low-Ti melt inclusions have lower Al_2O_3 (b), Na_2O (c), TiO_2 (f), and FeO (d) but higher CaO (e), SiO_2 (h), and $\text{CaO}/\text{Al}_2\text{O}_3$ (i) than normal inclusions. The low-Ti melt inclusions were not considered in this study due to their insignificant amounts.

The MIs analyzed in this study have only experienced post-entrapment crystallization of olivine because the MIs lack daughter minerals, have relatively constant $\text{CaO}/\text{Al}_2\text{O}_3$ ratios, and plot on a trend of olivine fractionation from the host glass (Fig. S2). This allows us to recovery primary melts through correcting the melt to be in equilibrium with the host by incrementally adding olivine using PETROLOG 3, assuming an Fe-Mg exchange efficiency of 0.3 (Danyushevsky and Plechov, 2011; Roeder and Emslie, 1970). All the corrected major element compositions of the MIs are relatively primitive ($\text{MgO} = 8\text{--}12$ wt%; Fig. S2) and plot on the trend defined by adding olivine to the host glass (Fig. S2).

Post-entrapment Mg–Fe exchange (i.e., “Fe-loss or Fe-gain”; Danyushevsky et al., 2000) between the MIs and host olivines is insignificant, as FeO_t contents of the MIs follow the olivine fractional crystallization trend from the host glasses (Fig. S2).

Before comparing the primary melts of the SCS MORBs with the global dataset, it is necessary to remove the effects of olivine fractionation on the major compositional variabilities of primary melts and global dataset. Therefore, we recalculated the major element contents of the MIs and glass to be in equilibrium with olivine with $\text{Fo} = 90$ mol% by incrementally adding olivine using PETROLOG 3, assuming an Fe-Mg exchange efficiency of 0.3 (Danyushevsky and Plechov, 2011; Roeder and Emslie, 1970).

3. Estimation of the Amount of Eclogite in the Mantle Source of SCS N-MORBs

Using Olivine Composition

The amount of eclogite in the mantle source of the SCS N-MORBs was estimated using the method of Sobolev et al. (2007). To ensure comparability between our estimation for SCS N-MORBs and that of global basalts, we adopted almost the same calculation steps and parameters as those of Sobolev et al (2007).

Mn/Fe ratios of the olivines and amount of the pyroxenitic end-member (X_{px}) yield a straight line:

$$X_{px} = 3.48 - 2.071 \times (100\text{Mn/Fe}) \quad (1)$$

We used Eq. [1] to calculate the amount of pyroxenitic end-member for each collected olivine composition from Yang et al. (2023), which yielded a mean value of 0.46 ± 0.07 (Fig. S3).

$$X_{crc} = \frac{X_e}{F_e \left(\frac{1-X_{px}F_{px}}{X_{px}F_{pe}} + \frac{1-F_eX_e}{F_e} + 1 \right)} \quad (2)$$

The amount of recycled oceanic crust (X_{crc}) was then estimated using Eq. [2] and the determined proportion of pyroxenite-derived melt (X_{px}), degree of melting of eclogite (F_e), amount of eclogite-derived melt needed to produce hybrid pyroxenite from peridotite (X_e), and degrees of melting of peridotite (F_{pe}) and pyroxenite (F_{px}).

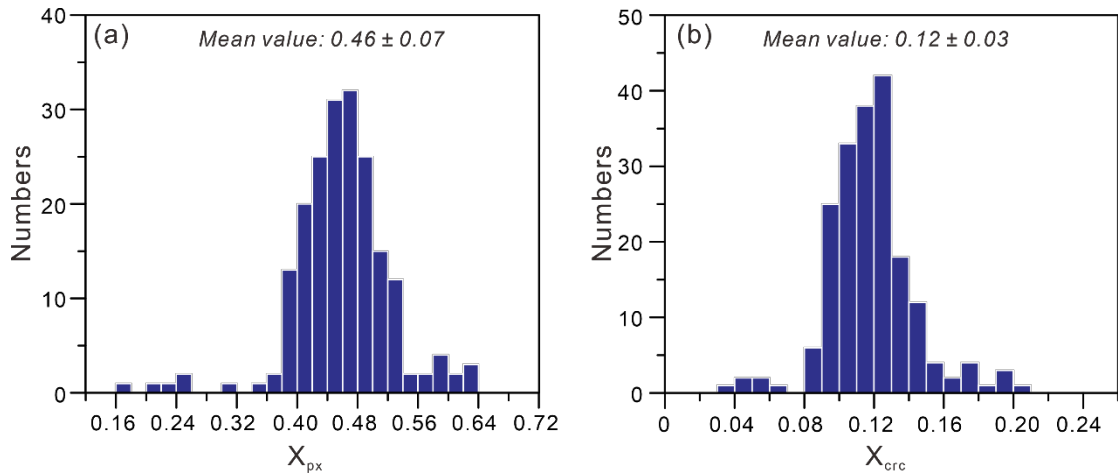


Figure S3. Data distribution of fractions of pyroxenite melts (X_{px}) and recycled oceanic crust (X_{cre})

Following Sobolev et al (2007), we assumed that the extent of eclogite melting reaches a maximum of 50%, which is unlikely to be significantly exceeded during fractional melting due to its highly refractory residue. We assumed 60% pyroxenite melting, as pyroxenite yields a maximum of ~60% melt during batch melting at 1 GPa and 1320–1350°C, based on the petrological modeling conducted by Sobolev et al (2007). In addition, we used the melt fraction of peridotite based on a published model (Sobolev et al., 2007) for MORBs (10%).

195 olivine grains from 15 samples of the upper section of U1431E MORBs gives 195 values (Yang et al., 2023) of the amounts of recycled oceanic crust (ROC) in the source, ranging from 3% to 20% with average $12\% \pm 3\%$ (Fig. S3). Such a value of ROCs in the source for the SCS is reasonably consistent with the fact the U1431E olivine has higher NiO than other MORBs (~4% ROC) but still lower than olivines from the within-plate basalts of thick lithosphere (~20% ROC) (Sobolev et al., 2007).

4. Numerical Modeling

We use a code written in MATLAB (LL_AM_TMM) to conduct the 2D numerical experiments (Liu et al., 2018a,b, 2019, 2024). The code is based on the Lagrangian-type finite element code MILAMIN. It includes a free surface on the top (a surface with no shear or normal stress) (Andrés-Martínez et al., 2015). The energy equation includes thermal diffusion, thermal convection, radioactive heating, and shear heating (viscous dissipation) (Eq. 3). The code describes viscoplastic deformation using the equations

of force balance and mass conservation (Eqs. 4-5). A detailed description of the numerical model can be found in [Liu et al. \(2018a,b, 2019\)](#).

$$\rho c_p \frac{dT}{dt} = \nabla \cdot (k \nabla T) + H \quad (3)$$

where ρ is the density (Eq. 6), c_p is the heat capacity, t is the time, k is the thermal conductivity, and H is the volumetric heat production rate (including both radioactive heating and viscous dissipation).

$$\nabla \cdot \vec{u} = 0 \quad (4)$$

$$-\nabla p + \nabla \cdot [\eta_{eff}(\nabla \vec{u} + \nabla^T \vec{u})] + \rho \vec{g} = 0 \quad (5)$$

In Eqs 4–5, \vec{u} refer to velocity components, p is the dynamic pressure, and g is the gravity acceleration.

The equation of state for density is:

$$\rho = \rho_c \cdot \exp \left[-\int_{T_0}^T \alpha(T) dT + \int_{P_0}^P \frac{dP}{K} \right] \quad (6)$$

$$\alpha = \alpha_0 + \alpha_1 T + \alpha_2 T^{-2}, \quad (7)$$

where ρ is the net density; α is the temperature-dependent thermal expansion coefficient; T_0 and P_0 are the room temperature and pressure, respectively; K is the bulk modulus; T and P are the temperature (in K) and pressure in the lithosphere, respectively; and α_0 , α_1 , and α_2 are constants. [Fig. S4](#) lists the model parameters.

k (Wm ⁻¹ K ⁻¹)	3.3
Hr (μW/m ³)	0.033
c_p J/(kg·K)	1200
ρ_0 (kg·m ⁻³)	3360
α_1 (10 ⁻⁴)	0.2697
α_2 (10 ⁻⁸ K ⁻¹)	1.0192
α_3 (K ²)	-0.1282
K (GPa ⁻¹)	134

Figure S4. Parameters used in the numerical model. k = thermal conductivity; Hr = radioactive heat production; c_p = heat capacity; ρ_0 = compositional density (Schutt and Lesher, 2006); α_1 – α_3 = constants for calculating the coefficient of thermal expansion (Djomani et al., 2001; Schutt and Lesher, 2006); K = bulk modulus. In Run 1, ρ_c is equal to ρ_0 ; in Runs 2–17, ρ_c is increased from $1.0006\rho_0$ to $1.0096\rho_0$ at $0.0006\rho_0$ increments.

Our 2-D model domain is a 3000 km wide \times 600 km deep box (Liu et al., 2019) (Fig. S5). The model adopts a mesh with adaptively refined triangular elements, with small elements (~ 5 km) near boundaries between different materials and large elements (~ 50 km) in regions far from internal material interfaces.

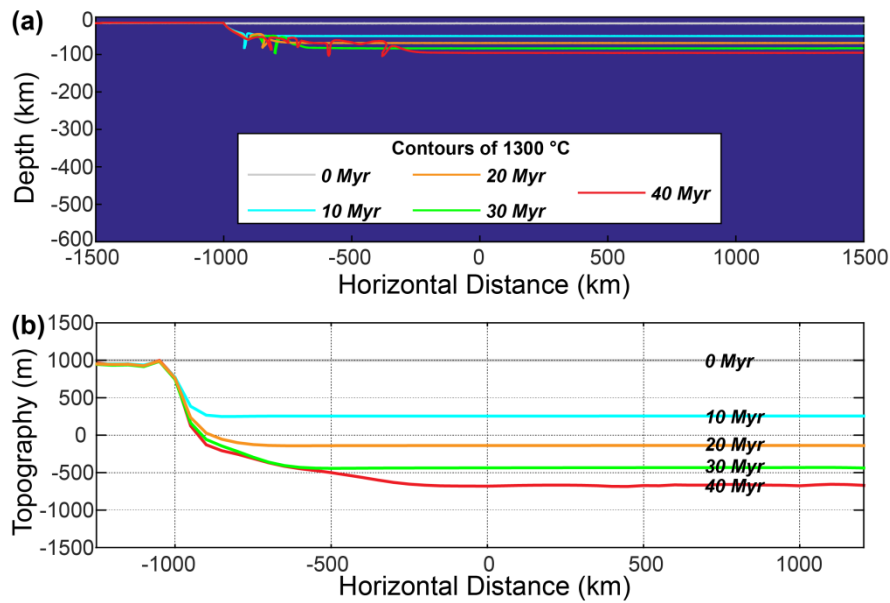


Figure S5. Numerical modeling of the growth of a thermal boundary layer (Run 1). (a) Model set-up and evolution of the thermal boundary layer. Colored lines are the contours for 1300 °C at 0, 10, 20, 30, and 40 Myr. (b) Evolution of surface topography relative to that of the left side of the model.

We assumed the mantle is an incompressible Stokes fluid. We utilized a free surface boundary condition (Andrés-Martínez et al., 2015) for the upper boundary and a free slip boundary condition for the other boundaries. The side walls have a zero heat flux condition. The surface temperature was set to 0°C, and at the base of the computational box was set to 1350°C. We simulated the growth of a thermal boundary layer from an initially hot asthenosphere with a uniform mantle temperature of 1350°C (Fig. S5). In the 2D model, the left 500 km of the surface remains at an initial temperature of 1350°C, while the rest of the surface cools to the top boundary at 0°C. This method of studying the growth of a thermal boundary layer is based on the analytical solution for a half-space cooling problem from Liu et al (2019) and Turcotte and Schubert (2014).

We simulate the growth of a thermal boundary layer from an initially hot asthenosphere with a uniform mantle temperature of 1350 °C (Figure S5), which has been benchmarked with an analytical solution for a half-space cooling problem (Liu et al., 2019). In the 2-D model, the left 500 km of the surface remains at the initial temperature of 1350 °C, while the rest of the surface cools down with the top boundary defined as 0 °C (Figure S5a). We track the differential subsidence of the growing thermal boundary relative to that of the left side (Figure S6) to explore the effects of the lithosphere's compositional density on the subsidence history.

Seventeen numerical models are presented here. In Run 1, the density of the newly formed lithosphere is the same as that of the ambient mantle (ρ_0 ; Fig. S6), while in Runs 2–17 the density is gradually increased from $1.0006\rho_0$ to $1.0096\rho_0$ at $0.0006\rho_0$

increments. The subsidence of the topography in each run is summarized in Fig. S6.

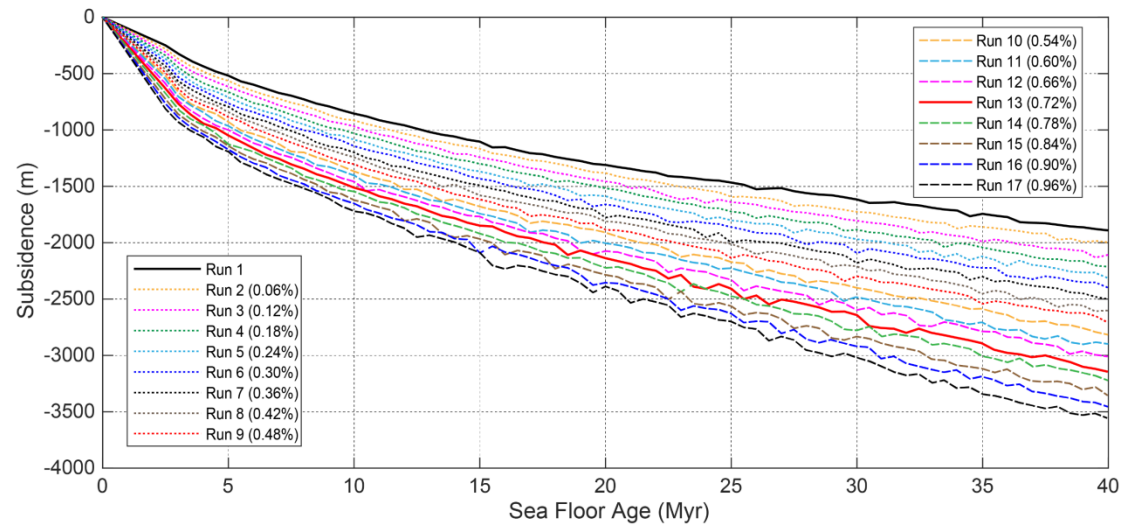


Figure S6. The modeled relative subsidence of the ocean floor. Run 1 is the reference model where the oceanic lithosphere has the same density as the ambient mantle (ρ_0). The density of the oceanic lithosphere increases from $1.0006\rho_0$ to $1.0096\rho_0$ in Runs 2–17. The numbers in parentheses represent the corresponding density increase (in %) for each run.

5. Additional Information on the Composition of the SCS MORBs and Their Mantle Source Lithology

The variations of major element composition with $\text{FeO}_t/\text{SiO}_2$ of primary melts recovered from MIs of olivines hosted by SCS MORBs provides additional supports for the requirement of the silica-deficient iron-rich pyroxenite for generating the SCS MORBs (Fig. S7). With mantle melting increasing, Na_2O , K_2O , TiO_2 decrease while CaO increases (Fig. S7). Melts of Si-rich pyroxenites including GV-10, M5-103, M5-40 (Lambart et al., 2009; Borghini et al., 2017) show similar major element composition

177 with the PE-melts including the MM3, pyrolite, sp-lherzolite ([Jaques and Green, 1980](#);
178 [Falloon et al., 2008](#)). Melts of silica-deficient iron-rich pyroxenite (M7-16) shows
179 distinguishably higher $\text{FeO}_t/\text{SiO}_2$ and lower SiO_2 than both PE and Si-rich pyroxenite
180 ([Fig. S7](#)). PE-melts cannot explain the high $\text{FeO}_t/\text{SiO}_2$ of the studied samples. The
181 mixing between PE-melts and melts of M7-16 explains the composition of the studied
182 samples.

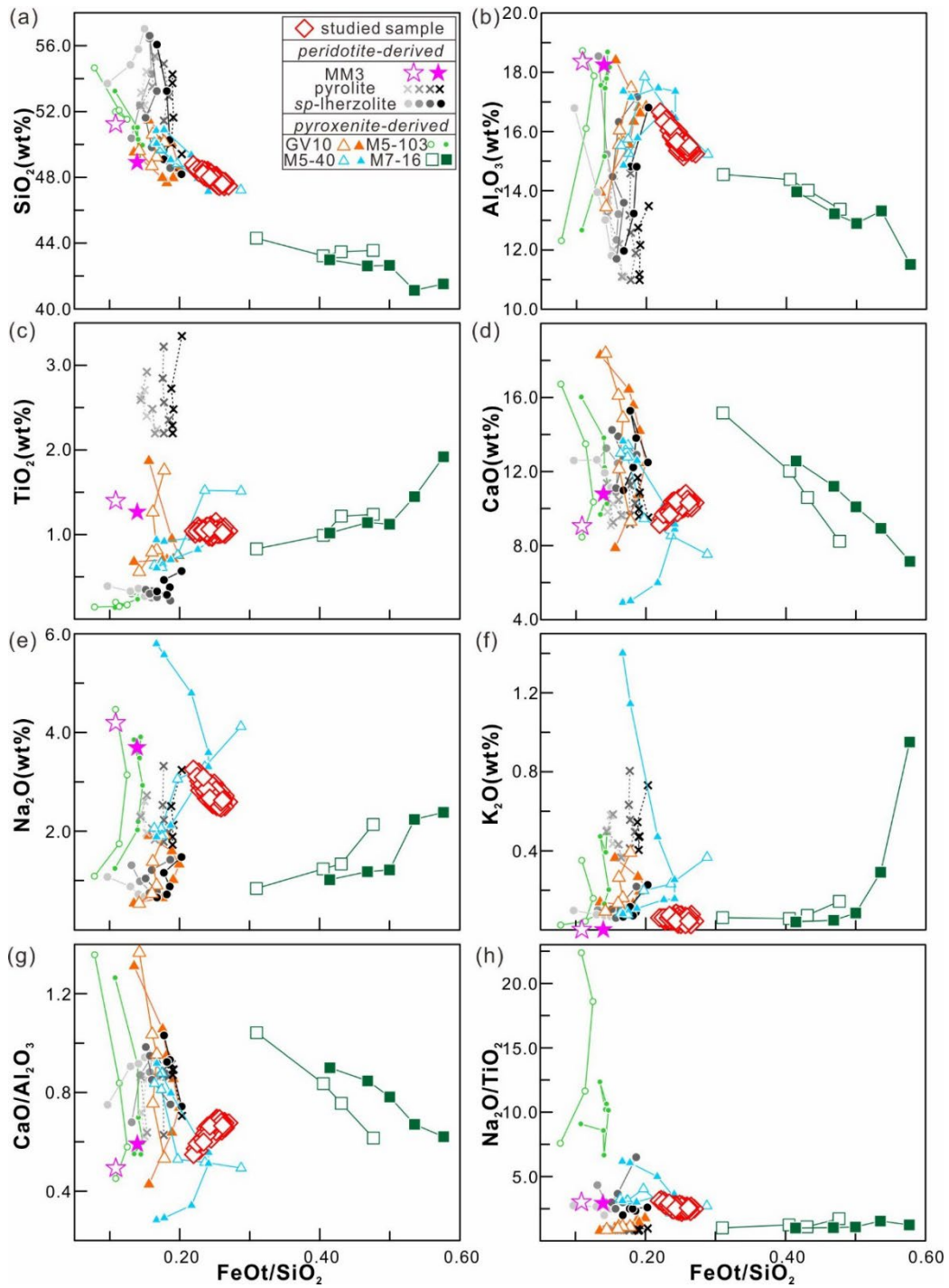


Figure S7. Plots of major element contents and ratios versus FeO/SiO_2 ratios for melt inclusions in the SCS MORBs. (a) SiO_2 , (b) Al_2O_3 , (c) TiO_2 , (d) CaO , (e) Na_2O , (f) K_2O , (g) $\text{CaO}/\text{Al}_2\text{O}_3$, (h) $\text{Na}_2\text{O}/\text{TiO}_2$. Melts from low-pressure melting experiments on peridotite (Jaques and Green, 1980; Falloon et al., 2008) and pyroxenite (Lambart et al., 2009; Borghini et al., 2017) are shown for comparison. All data of melt inclusions

has been corrected to be of $\text{MgO} = 10 \text{ wt } \%$.

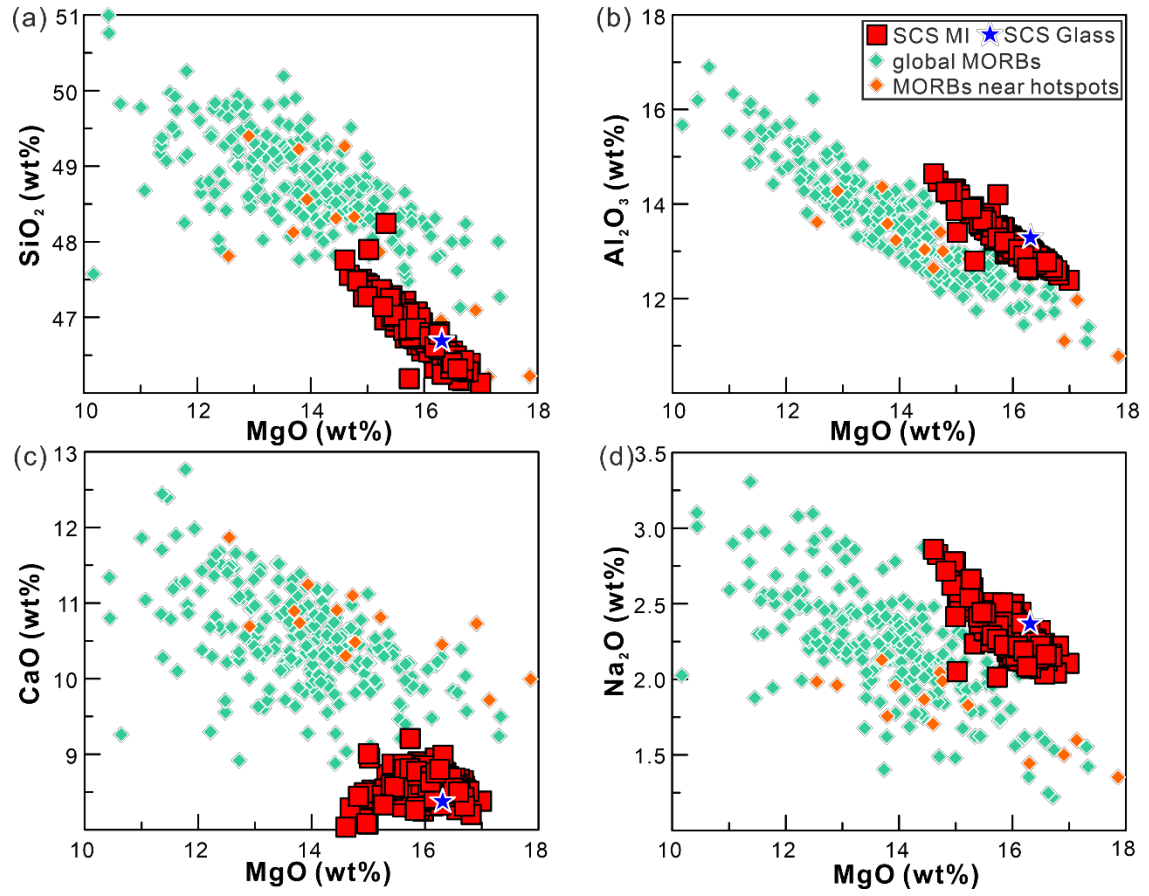


Figure S8. Comparison of primary melts of the SCS N-MORBs and global MORBs.

Data on global MORBs are from [Gale et al \(2014\)](#). All data are corrected to be in

equilibrium with olivine with $\text{Fo} = 90 \text{ mol } \%$.

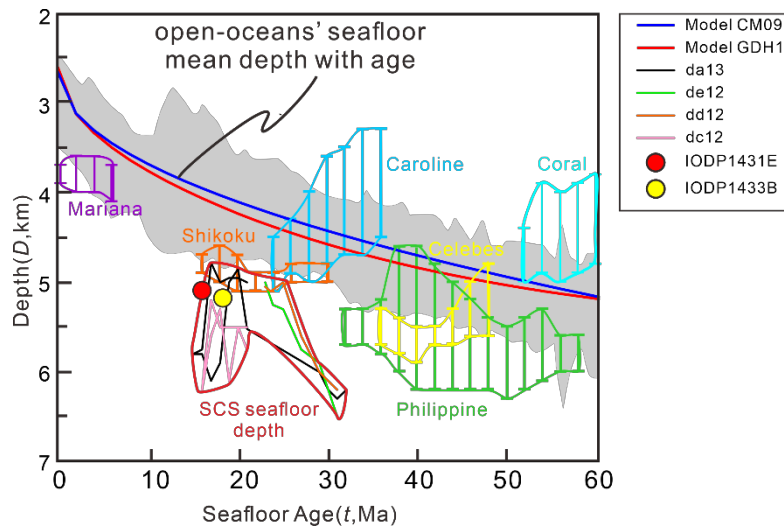


Figure S9. Age-Depth relationships for young oceanic basins. Refer to the main text for detail. This figure is presented as supplements for showing how the age-depth range for different basins is contoured (in Fig.1B).

Additional References

- Andres-Martinez, M., Morgan, J. P., Perez-Gussinye, M., and Rupke, L., 2015, A new free-surface stabilization algorithm for geodynamical modelling: Theory and numerical tests: Physics of the Earth and Planetary Interiors, v. 246, p. 41–51.
- Dabrowski, M., Krotkiewski, M. & Schmid, D., 2008, MILAMIN: MATLAB based finite element method solver for large problems: Geochem. Geophys. Geosyst. 9.
- Danyushevsky, L. V., and Plechov, P., 2011, Petrolog3: Integrated software for modeling crystallization processes: Geochemistry Geophysics Geosystems, v. 12.
- Danyushevsky, L. V., Della-Pasqua, F. N., and Sokolov, S., 2000, Re-equilibration of melt inclusions trapped by magnesian olivine phenocrysts from subduction-related magmas: petrological implications: Contributions to Mineralogy and Petrology, v. 138, p. 68–83.
- Djomani, Y. H. P., O'Reilly, S. Y., Griffin, W. L., and Morgan, P., 2001, The density structure of subcontinental lithosphere through time: Earth and Planetary Science Letters, v. 184, p. 605–621.
- Liu, L., Li, H.Y., Liu, L. et al., 2024, Horizontally forced initiation of the Izu-Bonin-Mariana subduction zone. Commun Earth Environ, v.5, 91.
- Liu, L., Morgan, J. P., Xu, Y. G., and Menzies, M., 2018, Craton Destruction 2: Evolution of Cratonic Lithosphere After a Rapid Keel Delamination Event: Journal of Geophysical Research-Solid Earth, v. 123, p. 10069–10090.
- Liu, L., Morgan, J. P., Xu, Y. G., and Menzies, M., 2018, Craton Destruction 1: Cratonic Keel Delamination Along a Weak Midlithospheric Discontinuity Layer: Journal of Geophysical Research-Solid Earth, v. 123, p. 10040–10068.
- Roeder, P. L., and Emslie, R. F., 1970, Olivine-Liquid Equilibrium: Contributions to Mineralogy and Petrology, v. 29, p. 275–289.
- Schutt, D. L., and Leshner, C. E., 2006, Effects of melt depletion on the density and seismic velocity of garnet and spinel lherzolite: Journal of Geophysical Research-Solid Earth, v. 111.
- Turcotte, D., and Schubert, G., 2014, Geodynamics: Cambridge, UK, Cambridge university press, 636 p.
- Yang, F., Huang, X.L., Xu, Y.G., and He, P.L., 2019, Plume-ridge interaction in the South China Sea: Thermometric evidence from Hole U1431E of IODP Expedition 349: Lithos, v. 324–325, p. 466–478.
- Zhang, L., Ren, Z.Y., Xia, X.P., Yang, Q., Hong, L.B., and Wu, D., 2019, In situ determination of trace elements in MIs using laser ablation inductively coupled plasma sector field mass spectrometry: Rapid Communications in Mass Spectrometry, v. 33, p. 361–370.